

A missense variant in the nuclear localization signal of DKC1 causes Hoyeraal-Hreidarsson syndrome

Chi-Kang TSENG (✉ ckt0513@ntu.edu.tw)

Department of Microbiology, College of Medicine, National Taiwan University,

Ni-Chung Lee

Department of Medical Genetics, National Taiwan University <https://orcid.org/0000-0002-5011-7499>

Chia-Mei Chu

Department of Microbiology, College of Medicine, National Taiwan University

Meng-Ju Tsai

Department of Pediatrics National Taiwan University Children's Hospital

Hsin-Hui Yu

Department of Pediatrics National Taiwan University Children's Hospital

En-Ting Wu

Department of Pediatrics National Taiwan University Children's Hospital

Yun-Li Yang

Department of Pediatrics National Taiwan University Children's Hospital

Chin-Hsien Lin

National Taiwan University Hospital <https://orcid.org/0000-0001-8566-7573>

Shin-Yu Lin

Department of Obstetrics and Gynecology, National Taiwan University Hospital

Yin-Hsiu Chien

Department of Medical Genetics, National Taiwan University Hospital <https://orcid.org/0000-0001-8802-5728>

Wuh-Liang Hwu

Department of Medical Genetics, National Taiwan University Hospital

Wen-Pin Chen

Institute of Pharmacology, College of Medicine, National Taiwan University

Article

Keywords: DKC1, hTR, PAPD5, Dyskeratosis congenita, Hoyeraal-Hreidarsson syndrome

Posted Date: May 31st, 2022

DOI: <https://doi.org/10.21203/rs.3.rs-1641825/v1>

License:  This work is licensed under a Creative Commons Attribution 4.0 International License.

[Read Full License](#)

Version of Record: A version of this preprint was published at npj Genomic Medicine on October 30th, 2022. See the published version at <https://doi.org/10.1038/s41525-022-00335-8>.

27 **Abstract**

28 Hoyeraal-Hreidarsson syndrome (HHS) is the most severe form of dyskeratosis
29 congenita (DC) and is caused by genes involved in telomere maintenance. Here, we
30 identified male siblings from a family with HHS carrying a hemizygous mutation
31 (c.1345C>G, p.R449G), located in the C-terminal nuclear localization signal (NLS) of
32 the *DKC1* gene. These patients exhibit progressive cerebellar hypoplasia, recurrent
33 infections, pancytopenia due to bone marrow failure, and short leukocyte telomere
34 lengths. Single-cell RNA sequencing analysis suggested defects in the NLRP3
35 inflammasome in monocytes and the activation and maturation of NK cells and B cells.
36 In experiments using induced pluripotent stem cells (iPSCs) from patients,
37 *DKC1_R449G* iPSCs had short telomere lengths due to reduced levels of human
38 telomerase RNA (hTR) and increased cytosolic proportions of *DKC1*. Treatment with
39 dihydroquinolizone RG7834 and cordycepin rescued telomere length in patient-derived
40 iPSCs. Together, our findings not only provide new insights into immunodeficiency in
41 DC patients but also provide treatment options for telomerase insufficiency disorders.

42

43

44

45

46 **Introduction**

47 *DKC1*, which encodes a nucleolar protein called DKC1 (dyskerin)¹, is the first gene
48 identified to play a role in dyskeratosis congenita (DC), which is a rare inherited disease
49 that is estimated to affect approximately one person per million people and is mainly
50 characterized by the triad of abnormal skin pigmentation, oral leucoplakia, and nail
51 dystrophy². Hoyeraal-Hreidarsson syndrome (HHS) is the most severe form of DC and
52 has a very early age of onset^{3,4}. Patients with HHS are characterized by very short
53 telomeres and manifest additional features compared to DC patients, such as cerebellar
54 hypoplasia^{3,4}. At the molecular level, DC/HHS patients have characteristic accelerated
55 telomere shortening^{2,5}. Mortality is primarily caused by recurrent infection due to
56 progressive bone marrow failure with compromised immune function². A therapeutic
57 strategy for telomere disorder-related diseases remains to be developed.

58 **Results**

59 We identified siblings from a family with HHS. Whole-exome sequencing (WES)
60 of the index patient identified a hemizygous c.1345C>G (p.R449G) variant in the *DKC1*
61 gene (NM_001363) (**Supplementary Fig. 1a**). This missense variant was considered to
62 be disease-causing (ClinVar variation ID: 235576), with an ACMG classification of
63 likely pathogenic (PS3 PM2 PP1 PP2 PP3 PP4). Sanger sequencing confirmed that the
64 elder brother had the same hemizygous variant, while the mother was a carrier (**Fig. 1a**

65 and **Supplementary Fig. 1b**). The patient's mother had a brother who died at 3 years of
66 age for unknown reasons (**Fig. 1a**). The telomere lengths in gDNA from circulating
67 leukocytes of the siblings were shorter than those of age-matched controls in a
68 quantitative PCR assay (**Fig. 1b**).

69 The elder brother presented with intrauterine growth restriction, developmental
70 delay, cerebellar hypoplasia (**Fig. 1c**), and hepatosplenomegaly (**Fig. 1d**) since the ages
71 of 1 year and 4 months. Severe aplastic anaemia with progressive pancytopenia developed
72 at the ages of 2 years and 6 months. He died at 3 years old due to *Burkholderia*
73 *cenoepecia* bacteremia and *Pneumocystis jiroveci* pneumonia (PJP) complicated with
74 severe acute respiratory distress syndrome (ARDS) (**Supplementary Table 1**). The index
75 patient manifested developmental delay, ataxia, cerebellar hypoplasia (**Fig. 1e**),
76 hepatosplenomegaly (**Fig. 1f and 1g**), progressive leukopenia, lymphopenia, and
77 thrombocytopenia since he was 1.6 years of age, and anaemia and leukopenia since he
78 was 3.5 years of age. He had recurrent viral (adenovirus pneumonia with severe ARDS,
79 herpes simplex virus), bacterial (*Acinetobacter baumannii*), and fungal (PJP, *Candida*
80 *albicans*) infections since he was 2.8 years old despite regular intravenous
81 immunoglobulin (IVIG) administration and prophylactic antimicrobial agent usage. He
82 died at 5.7 years of age due to PJP with respiratory failure.

83 Immunological studies for the index patient revealed decreased T, B, and NK
84 lymphocytes, normal IgG and IgA levels, and transient elevation of IgM levels
85 (**Supplementary Table 1**). To dissect complex immune cell functions in healthy
86 individuals and DCs, single-cell RNA sequencing (scRNA-seq) was performed on
87 PBMCs from the index patient (DC) and the age-matched healthy donor (HD) (**Fig. 2a**).
88 Five major clusters (B cells, CD4⁺ T cells, CD8⁺ T cells, monocytes, and NK cells) were
89 clustered based on known cell-type-specific gene profiles⁶ (**Fig. 2a**). The results indicated
90 that the size of the monocyte population was increased. However, there were reductions
91 in the proportions of B cells, CD4⁺ T cells, CD8⁺ T cells, and NK cells (**Fig. 2b**).

92 An integrated analysis of PBMCs was performed. Reactome analysis indicated that
93 immune system- and anti-pathogen-related pathways were enriched (**Fig. 2c**). Genes
94 involved in the anti-microbial response were upregulated, including IFN-related genes
95 (*IFNAR1*, *JAK1/2*, *TYK2*, *STAT1/2*), genes involved in the OAS/RNase L pathway (*OAS1*,
96 *PAS2*, *OAS3*, *OASL*, and *RNase L*), and the RNA sensor DDX58 (*RIG-I*) (**Fig. 2d**).
97 Additionally, interferon-stimulated genes (ISGs) and interferon-inducible (IFI) genes
98 were upregulated (**Fig. 2d**). The expression of anti-apoptotic survival factors, such as
99 *STAT5A* and *BCL-2*, was increased (**Fig. 2d**). Expression of the pleiotropic immune
100 modulator *LGALS9*, which encodes Galectin-9 (Gal-9), was increased in all cells⁷ (**Fig.**
101 **2d**).

102 The expression levels of IFN- γ (*IFNG*) and genes involved in the expression of IFN-
103 γ (*FOS*, *JUN*, *TBX21*) were reduced (**Fig. 2d**). IFN- γ is a critical cytokine that activates
104 macrophages and links the innate and adaptive immune responses⁸. We also observed
105 reductions in the expression levels of NF- κ B genes (*NFKB1* and *NFKB2*), which are
106 crucial regulators of inducible gene expression involved in the development and function
107 of immune cells⁹. Overall, the integrated analysis of single-cell RNA-seq data from
108 PBMCs in combination with recurrent and opportunistic infections at initial presentation
109 suggested that the immune system of the DC patient was dysfunctional.

110 A large proportion of monocytes was observed in the DC patient (**Fig. 2b**). To
111 examine the function of monocytes, three distinct monocyte subsets were grouped
112 according to the expression of CD14 and CD16: classical monocytes (CD14^{hi}CD16⁻),
113 intermediate monocytes (CD14^{hi}CD16⁺), and nonclassical monocytes (CD14^{Low}CD16^{hi})
114 (**Fig. 3a**). Monocytes egress from the bone marrow as classical monocytes
115 (CD14^{hi}CD16⁻), and a portion of them subsequently differentiate into intermediate
116 monocytes (CD14^{hi}CD16⁺) and nonclassical monocytes (CD14^{Low}CD16^{hi})¹⁰.
117 Nonclassical monocytes have been suggested to represent an aged monocyte subset due
118 to detection of several ageing markers, such as short telomere length¹¹ and high
119 expression levels of CX3CR1¹². Since the DC patient exhibited shorter telomeres than
120 the age-matched control (**Fig. 1g**), we examined the monocyte ageing marker CX3CR1.

121 CX3CR1 was highly expressed on three types of monocytes from the DC patient (**Fig.**
122 **3b**), suggesting that monocytes derived from the DC patient prematurely undergo the
123 ageing process.

124 In contrast to nonclassical monocytes, classical monocytes exhibit high
125 expression of genes involved in responses to bacterial infection and inflammation and
126 genes involved in inflammasome signalling¹³. In DC patients, reductions in the proportion
127 of classical monocytes (**Fig. 3a**) and the expression levels of NF- κ B (**Fig. 2b**), which is
128 a transcription factor for many proinflammatory cytokines, prompted us to speculate that
129 proinflammatory cytokine production/secretion was impaired in the DC patient. As
130 expected, the expression levels of genes involved in NLRP3 inflammasome formation¹⁴
131 (*NLRP3*, *IL1 β* , *IL-18*, *TNF*, *NFKB1*, and *NFKB2*) were dramatically decreased (**Fig. 3b**).
132 The NLRP3 inflammasome triggers caspase-1 activation and secretion of the
133 proinflammatory cytokines IL-1 β and IL-18¹⁵. IL-18 is essential for IFN- γ production,
134 which augments the cytotoxicity of NK cells and T cells¹⁶. Low expression levels of
135 NLRP3 inflammasome-related genes (**Fig. 3b**) and IFN- γ (**Fig. 2d**) suggest that
136 downstream immune responses are defective.

137 We grouped NK-cell subsets. The proportion of immature CD56^{bright} NK cells,
138 which normally represent a maximum of 10% of all peripheral blood NK cells, was
139 increased (15.8%) concomitant with a decrease in the proportion of CD56^{dim} NK cells

140 (84.2%) (**Fig. 3c**). The DC patient displayed high expression levels of CD56, the major
141 inhibitory receptor (*CD94* and *NKG2A*), the activating receptor NCR1 (*NKp46*), the
142 cytokine receptor *IL18RAP*, and the adhesion molecule CD2 but low expression levels of
143 *CD160*, which is mainly expressed by CD56^{dim} NK cells¹⁷. The expression levels of
144 *LGALS9*, which has been shown to impair NK-cell functions by affecting cell-mediated
145 cytotoxicity and decreasing IFN- γ production, were increased¹⁸ (**Fig. 3d**).

146 T- and B-cell immunodeficiency was the predominant finding in DKC patients at
147 initial presentation (**Supplementary Table 1**). Next, we analysed T and B cells in DC
148 samples. The proportions of CD4⁺ and CD8⁺ T cells were not substantially different
149 between the healthy donor and DC patient (**Fig. 4a**). Additionally, the expression of genes
150 encoding exhaustion markers (*PD-1*, *LAG3*, *CTLA-4*, *TIGIT*, *KLRG1*) on T cells was not
151 significantly different (data not shown). However, the DC patient showed a high
152 percentage of naïve B cells (90%) (**Fig. 4b**). Supporting this observation, B cells from the
153 DC patient showed high expression levels of a naïve B-cell marker (*TCL1A*) and *LGALS9*
154 but low expression levels of *CD19*, *CCR7* and *CXCR5*. The threshold for B-cell receptor
155 signalling pathways is mediated by *CD19*¹⁹. *CCR7* and *CXCR5* direct circulating B cells
156 into secondary lymphoid tissues, where they can be activated by antigens. In contrast, the
157 expression of genes involved in B-cell activation (*CD83*, *Jun*, *JunB*, *Fos*, *FosB*, *ICOSLG*,
158 *STAT3*, *CD44*, *NR4A1*) and B-cell proliferation (*EGR-1*) was abolished or dramatically

159 downregulated, suggesting that B cells from DC patients have defects in activation,
160 homing, or maturation (**Fig. 4d**).

161 A missense variant (c.1345C>G) of *DKC1* resulted in the substitution of a highly
162 conserved amino acid, p.Arg449Gly, which is localized in the conserved nuclear
163 localization signal domain of *DKC1* (**Supplementary Fig. 2**). *DKC1* is required for the
164 stability and maturation of hTR²⁰⁻²². To study the effects of the *DKC1* alterations on
165 telomere maintenance, iPSCs were generated from the PBMCs of the index patient and
166 his father. We obtained one clone (WT_iPSC_F) of iPSCs from the patients' father and
167 two independent clones (R449G_iPSC_1 and 2) of iPSCs from the younger patient.
168 Compared to iPSCs derived from a healthy donor (WT_iPSCs), all the iPSCs we
169 reprogrammed showed all the hallmarks of pluripotency, including characteristic
170 morphology (**Supplementary Fig. 3a**) and gene expression (**Supplementary Fig. 3b**).
171 Sanger sequencing analysis showed that both R449G_iPSC_1 and R449G_iPSC_2 but
172 not WT_iPSC and WT_iPSC_F contained the c.1345C>G variant in *DKC1*
173 (**Supplementary Fig. 3c**). Karyotype analysis of WT_iPSC, WT_iPSC_F, and
174 R449G_iPSC_1 was normal and revealed 46 chromosomes with X and Y. However,
175 R449G_iPSC_2 had an abnormal chromosome karyotype at r(18) (p11.31q21.1), a
176 feature of chromosomes with dysfunctional telomeres (**Supplementary Fig. 3d**).

177 The telomere lengths of R449G_iPSC_1 and R449G_iPSC_2 (**Fig. 5a, lanes 7~12**)
178 were shorter than those of WT_iPSC and WT_iPSC_F (**Fig. 5a**). DKC1_R449G mutant
179 iPSCs did not show significant reductions in the levels of key protein components of
180 telomerase, including TERT, DKC1, NHP2, and NOP10 (**Fig. 5b**), but showed a dramatic
181 70% reduction in the steady-state level of hTR (**Fig. 5c**). Cell fractionation of iPSCs
182 revealed that the cytoplasmic proportions of DKC1 and other core H/ACA components
183 (NHP2 and NOP10) increased in both R449G_iPSC_1 and R449G_iPSC_2 compared to
184 WT_iPSC and WT_iPSC_F (**Fig. 5d**). The localization of DKC1_R449G was further
185 confirmed by an immunofluorescence assay (**Fig. 5e and 5e**). Compared to WT_iPSC_F,
186 the cytoplasmic proportion of DKC1_R449G was increased by more than 3-fold in
187 R449G_iPSC_1 (**Fig. 5e and 5e**). These data suggest that the DKC1_R449G variant
188 causes mislocalization of DKC1 to the cytoplasm, leading to reduced levels of hTR and
189 telomere shortening.

190 Inhibition of PAPD5-mediated oligoadenylation has been suggested to be a means
191 of lengthening telomere length^{20,23-26}. Therefore, we treated R449G_iPS cells with
192 RG7834, a PAPD5 inhibitor, or cordycepin (3' deoxyadenosine). RG7834 was previously
193 reported to reverse the molecular cause of DC, increase hTR levels and lengthen
194 telomeres in iPSCs carrying DKC1 mutations^{26,27}. Cordycepin could induce chain
195 termination due to the absence of a 3' hydroxyl moiety and therefore terminate poly (A)

196 tail formation²⁸. Analysis of hTR purified from RG7834- or cordycepin-treated
197 WT_iPSC_F and R449G_iPSC_1 demonstrated minor effects on the steady-state levels
198 of hTR (**Fig. 6a**) but caused a reduction in the fraction of oligoadenylated hTR (**Fig. 6b**),
199 suggesting that PAPD5-mediated oligoadenylation was impaired. Remarkably, both
200 RG7834 and cordycepin partially restored telomere length in R449G_iPSC_1 (**Fig. 6c**,
201 **lanes 7 and 8**). These data suggest that the inhibition of oligoadenylation mediated by
202 PAPD5 is a strategy to attenuate telomere shortening caused by telomerase dysfunction.

203 **Discussion**

204 In summary, our data indicate that the NLS domain of DKC1 is important for
205 telomerase accumulation and telomere maintenance. A missense variant (R449G) causes
206 Hoyeraal-Hreidarsson syndrome. Biogenesis of human telomerase and degradation of
207 hTR undergo kinetic competition, which determines telomere length homeostasis (**Fig.**
208 **6d**). The DKC1_R449G variant results in the cytoplasmic accumulation of DKC1,
209 causing reduced levels of hTR and telomere shortening (**Fig. 6d**). Our data suggest that
210 cordycepin, like RG7834 (a PAPD5 inhibitor), blocks oligoadenylation of hTR, which is
211 targeted by the RNA exosome for degradation, and restores telomere length in patient-
212 derived iPS cells, suggesting that cordycepin could be a promising compound for
213 telomere-targeted therapy. Further studies are still needed to examine the effects of these
214 small compounds on telomere disorder syndrome and age-related degenerative disease.

215 We examined the transcriptomic profiles of immune cells in a DC patient carrying a
216 missense mutation (c.1345C>G) in the conserved nuclear localization signal domain of
217 *DKC1* using single-cell RNA-seq. We found that the DC patient exhibited immunological
218 features of defective NLRP3 inflammasomes in monocytes, immature NK dominance
219 with fewer cytotoxic NK cells (CD56^{dim} NK cells), and defective B-cell activation or
220 maturation, suggesting that the causes of poor immune responses in the DC patient are
221 caused by not only leukopenia but also dysfunction of immune cells. The NLRP3
222 inflammasome plays a crucial role in modulating the caspase-1-dependent release of
223 proinflammatory cytokines, which in turn controls the early phase of host defence,
224 inflammation and subsequent activation of adaptive immunity. To our knowledge, this is
225 the first report of a clinical phenotype showing loss of function of NLRP3. Interestingly,
226 the human NLRP3 gene resides in the subtelomeric region of chromosomes that are
227 deficient in DNA repair mechanisms. Severe loss of telomeres leads to end joining, as
228 shown by R449G_iPSC_2 (**Supplementary Fig. 3d**), which could cause damage to
229 essential genes, such as NLRP3. There are several limitations of our study. Our sample
230 size was small, and patients varied with respect to the timing of clinical presentation
231 during the progression of disease, which could influence the transcriptional landscape.
232 Whether NLRP3 deficiency in Hoyeraal-Hreidarsson syndrome could be a novel
233 component of innate immunity defects remains to be investigated.

234 **Methods**

235 **Ethical approval**

236 The study was approved by the Institutional Review Board of National Taiwan University
237 Hospital (IRB No. 201703073RINB and 201910057RIND). Written informed consent
238 was obtained from all subjects or their guardians.

239 **Exome sequencing**

240 Whole-exome sequencing (WES) was performed as previously reported²⁹. In brief, after
241 DNA extraction, exome capture was performed with the TruSeq Exome Capture Kit
242 (Illumina), and sequencing for the three participants (patient and both parents) was
243 conducted using the NextSeq500 mid output system (Illumina) with a 75-bp paired-end
244 run. The sequences were aligned to the human reference genome (GRCh37), and variant
245 calling was performed using the Genome Analysis Toolkit (GATK V3.5, Broad
246 Institute)³⁰. Variants were first annotated by Variant Studio (V3.0, Illumina) and
247 wANNOVAR (<http://wannovar.wglab.org/>)³¹. Candidate variants were checked with
248 ClinVar (<https://www.ncbi.nlm.nih.gov/clinvar/>). The pathogenicity of variants was
249 classified according to the ACMG guidelines³².

250 **Karyotype analysis**

251 Karyotype analysis of iPSCs was conducted as follows: iPSCs that reached eighty percent
252 confluence in 35 mm dishes were harvested after adding 10 µL of colcemid for 15 hours.
253 Then, 2 ml 0.28% KCl was added twice for 50 minutes. Then, 2 mL methanol/acetic acid
254 (3/1) was added for fixation. G banding was stained using 0.25% trypsin followed by
255 Wright's solution (pH 7.0 Gurr buffer/Wright's=3/1).

256 **iPSC derivation, culture, and drug treatment**

257 PBMCs from whole blood were separated by Ficoll-Hypaque density gradients and stored
258 in liquid nitrogen. iPSCs were derived from the PBMCs of the patient and the patient's
259 father. PBMCs were reprogrammed using Sendai virus according to the manufacturer's
260 instructions. For feeder-free culture, iPSCs were maintained in StemFlex completed
261 medium containing StemFlex™ Basal Medium (Gibco, Cat. No. A33493-01) and
262 StemFlex™ Supplement (10X) (Gibco, Cat. No. A33492-01) on Matrigel hESC-qualified
263 Matrix (Corning, Cat. No. 354277) at 37°C in a humidified atmosphere containing 5%
264 CO₂. To prepare Matrigel-coated dishes, Matrigel hESC-qualified matrix supplemented
265 with 25 mL of DMEM/F-12, HEPES (Gibco, Cat. No. 11330032) was added to 6-well
266 plates (1 mL/well) or 100 mm dishes (7 mL/dish) and incubated at 37°C for 2 hours.
267 iPSCs were subcultured when the cells were in log phase, and the cells were detached by
268 using Accutase® (Innovative Cell Technologies, Inc., Cat. No. #AT-104) and incubated
269 in an incubator at 37°C and 5% CO₂ for 5 min. The detached cells were centrifuged at
270 1000 rpm (Kubota 2010 tabletop centrifuge) for 5 min. Before seeding the cells, Matrigel
271 matrix supplemented with DMEM/F-12 was aspirated from the culture dish. iPSCs were
272 seeded on a Matrigel-coated dish containing StemFlex complete medium and 10 μM Y-
273 27632 dihydrochloride (Rock inhibitor) (Sigma–Aldrich, Cat: Y0503-5MG) at 37°C with
274 5% CO₂, and then the medium was changed every day. For RG7834 and cordycepin
275 treatment, iPSCs were maintained in StemFlex complete medium with 1 μM RG7834
276 (MedChemExpress (MEC), Cat. No.: HY-117650A), 1 μM Cordycepin
277 (MedChemExpress (MEC), Cat. No.: HY-N0262) or dimethyl sulfoxide (Sigma–Aldrich,
278 Cat: D4540-100ML) as a control on Matrigel hESC-qualified matrix. The cells were
279 subcultured as mentioned before.

280 **DNA sequencing and genetic analysis**

281 DNA sequencing of gDNA from PBMCs and iPSCs from healthy donors and DC patients
282 was performed by polymerase chain reaction (PCR) amplification of the specific region
283 of exon 14 for *DKC1*. The primers used for PCR and Sanger sequencing are listed in
284 **Supplementary Table 2**. Each PCR (100 μ l) contained 100 ng of DNA, 1X KAPA HiFi
285 Fidelity Buffer, 0.3 mM KAPA dNTP, 0.3 μ M each primer, and 0.005 U/ μ l KAPA HiFi
286 DNA Polymerase (Kapa Biosystems, Cat: KK2102). The reactions were carried out in a
287 T100TM Thermal Cycler (Bio Rad) under the following conditions: one cycle at 95°C for
288 3 min, followed by 30 cycles of 20 s at 98°C, 15 s at 50°C and 30 s at 72°C, with a final
289 cycle at 72°C for 1 min. PCR products were purified using a PCR extraction kit (TOOLS,
290 Cat: TT-B14-3) according to the manufacturer's instructions.

291 **Genomic DNA extraction and qPCR**

292 Genomic DNA was prepared from iPSC pellets (5×10^6 cells) with GenEluteTM
293 Mammalian Genomic DNA Miniprep Kits (Sigma–Aldrich, Cat. No: G1N350-1KT)
294 according to the manufacturer's instructions. To evaluate telomere lengths, polymerase
295 chain reaction (PCR)-based telomere length analysis methods have been developed. In
296 this study, telomere length was quantified by comparing the amount of the telomere
297 amplification product (T) to that of a single-copy gene (S, 36B4). The T/S ratio was then
298 calculated to yield a value that correlated with the average telomere length. Each reaction
299 contained 5 ng/ μ l genomic DNA or standard templates mixed with iQTM SYBR® Green
300 Supermix (Bio–Rad, Cat. No. 1708882) and primers. qPCR was performed in a CFX96TM
301 Real-Time System, C1000 TouchTM Thermal Cycler (Bio–Rad), with the following
302 cycling conditions: initial denaturation at 95°C for 10 min and 40 cycles at 95°C for 15
303 sec and 60°C for 1 min. Graphing and statistical analysis of qPCR results were performed
304 using Prism 8 (GraphPad). Standard telomere oligonucleotides, standard single-copy

305 gene (36B4) nucleotides, and primers used for qPCR are listed in **Supplementary Table**
306 **3**.

307 **Terminal restriction fragment (TRF) analysis**

308 Genomic DNA (2.2 µg) from iPSCs was digested with *Hinf* I (New England Biolabs, Cat.
309 No: #R0155S) and *Rsa* I (New England Biolabs, Cat. No: #R0167L) restriction enzyme
310 in 10X CutSmart® Buffer (NEB, Cat. No: #B7204S) at 37°C overnight. The digested
311 gDNA fragments were separated on a 1% SeaKem® LE agarose gel (Lonza, Cat. No:
312 50002) by electrophoresis at 120 V for 12 hr, followed by capillary transfer to a
313 Hybond™-N⁺ nylon transfer membrane (GE Healthcare, Cat. No: RPN303B) in 10X SSC
314 for 14.5 hr. DNA was subsequently crosslinked to the membrane twice at 120 mJ in a UV
315 Stratalinker 1800 (Stratagene, 254 nm, 120 mJ). The blot was prehybridized in Church
316 buffer at 65°C for an hour and then hybridized with ³²P-dCTP-labelled (TTAGGG)₃
317 overnight. The blot was exposed to a phosphor image screen (Fujifilm) at room
318 temperature overnight. Phosphor images were obtained with an Amersham Typhoon 5
319 scanner (Cytiva). The telomere length images were quantified and analysed by
320 ImageQuantTL software (Cytiva).

321 **Single-cell RNA sequence capture, library construction and sequencing**

322 Single-cell capture and downstream library construction were performed using
323 Chromium Next GEM Single Cell 3' Reagent Kits v 3.1 (10x Genomics; PN-1000121,
324 PN-1000127 and PN-1000213) for PBMCs from the DC patient and age-matched
325 controls, according to the manufacturer's protocol. Briefly, a total of approximately 8600
326 single cells, 50 µl of barcoded gel beads and 45 µl partitioning oil were loaded into
327 Chromium Next GEM Chip G to generate nanoliter-scale gel beads-in-emulsion (GEMs).
328 Afterwards, the polyadenylated mRNAs were reverse transcribed inside each GEM, and
329 the full-length cell-barcoded cDNA was amplified via PCR to generate sequencing

330 libraries. Library quality was assessed by using the Qubit 4.0 Fluorometer (Thermo
331 Scientific) and a Qsep100™ system (Bioptic, Taiwan) to determine the library
332 concentration and library size, respectively. In general, fragments of approximately 450-
333 500 bp in size were expected for single-cell 3' gene expression libraries. The effective
334 concentrations of the library were assessed by Q-PCR. The qualified libraries were pooled
335 according to the effective concentration and expected data volume. The library was
336 sequenced on Illumina NovaSeq 6000 sequencers according to read length: 28 bp Read 1
337 (16 bp single-cell barcode, 10x barcode; 12 bp unique molecular identifier, UMI), 91 bp
338 Read 2 (transcript insert or feature barcode in the case of the cell hashing library), and 8
339 bp i7 Index (sample index). TruSeq Read 1 and TruSeq Read 2 are standard Illumina
340 sequencing primer sites used in the paired-end sequencing of single-cell 3' gene
341 expression libraries.

342 **Single-cell gene expression analysis**

343 In the Chromium Single-Cell Software Suite, Cell Ranger (*cellranger count*) was used to
344 perform sample demultiplexing and generate feature-barcode matrices. Sequences were
345 mapped onto the human reference genome (GRCh38) provided by 10X Genomics.
346 Multiple samples were aggregated by “*cellranger aggr*” without depth normalization.
347 Unique molecular identifier (UMI) count matrices were imported into R (v3.6.0) and
348 processed with the R package Seurat (v3.2.1)^{33,34}. Log-normalized expression values
349 were obtained by the “*NormalizeData*” function of the Seurat package. Specifically,
350 “*LogNormalize*” was set by default in this function, and the gene counts for each cell were
351 divided by the total counts and multiplied by the *scale.factor* (default = 10,000) and then
352 natural-log transformed. Further analysis, including quality control, the identification of
353 highly variable genes (HVGs), dimensionality reduction, and standard unsupervised
354 clustering algorithms, was performed using the Seurat package. Cells were filtered out

355 before downstream analysis if (1) the percentage of mitochondrial genes was > 20% or
356 (2) the number of genes was < 200 or > Q3 + 1.5 IQR of the population. HVGs, which
357 are often used to keep the most informative variations in the scRNA-seq data^{35,36}, were
358 set in the “*FindVariableFeatures*” function of the Seurat package; the number of HVGs
359 was defined by the median gene number in the population, while “*nfeatures = 2,000*” was
360 defined if the median was below 2,000. Visualizing a high-dimensional single-cell dataset
361 is critical for interpretation of the results. Cell clustering was performed by using
362 dimensional reduction techniques and t-distributed stochastic neighbour embedding
363 (tSNE)^{37,38}. Note that in Seurat, both tSNE and UMAP were performed after PCA
364 (“*RunPCA*” function). The “*RunTSNE*” and “*RunUMAP*” functions in Seurat were set
365 with “*dims = 1:20*”. To evaluate the batch effect, batch mixing was used to quantify the
366 extent of intermingling of cells from different batches^{39,40}. If necessary, the mutual nearest
367 neighbour (MNN)³⁹ method was used for batch effect correction with the “*fastMNN*”
368 function of SeuratWrappers (v0.3.0). To identify the cell types captured by scRNA-seq
369 in an unbiased fashion, an automatic annotation method, SingleR (v1.0.1), was
370 performed⁴¹; this method correlates each cell with reference transcriptomic datasets
371 independently. Differentially expressed gene (DEG) analysis of the two conditions was
372 performed in Python using sSeq⁴² (total UMI count < 900) and edgeR^{43,44} (total UMI
373 count > 900), which is based on negative binomial distribution and asymptotic beta
374 testing, respectively⁴²⁻⁴⁴. We followed the method as stated in Cell Ranger and the Loupe
375 Cell Browser, and the source code is available in the 10X Genomics GitHub repository
376 (<https://github.com/10XGenomics/cellranger>).

377 **RNA extraction and reverse transcription PCR**

378 Total RNA was isolated from the iPSC pellets (1×10^7 cells) using Ambion TRIzol[®]
379 Reagent (Life Technologies, Cat. No: 15596018) according to the manufacturer’s

380 instructions, followed by DNase I (New England Biolabs, Cat: M0303 L) treatment at
381 37°C for 60 min. For cDNA synthesis, the reverse transcription reaction was performed
382 according to the manufacturer's instructions of the SuperScript™ IV First-Strand
383 Synthesis System (Thermo Fisher Scientific, Cat. No. 18091050). In brief, 2 µg of total
384 RNA was primed with 50 µM Oligo d(T)₂₀ primer or 50 ng random hexamers in 10 mM
385 dNTP mix and DEPC-treated water. PCRs were carried out in a T100™ Thermal Cycler
386 (Bio Rad) under the following conditions: one cycle at 65°C for 5 min and 4°C for 1 min.
387 Then, 1 µl of SuperScript™ IV RT was added to the reaction mixture containing
388 ribonuclease inhibitor (TOOLS, Cat: TTG-RI01), 5 mM DTT and 1X SSIV Buffer,
389 followed by incubation at 50°C for 1 hr, 80°C for 10 min, 37°C for 1 min and 4°C for 1
390 min. Finally, 1 µl of RNase H (2 U/µl) was added to the samples to remove RNA at 37°C
391 for 20 min, 65°C for 10 min, and 4°C for 10 min. RT-PCR was performed with primers
392 targeting pluripotent stem cell markers (OCT4, SOX2, NANOG) using a standard Taq
393 Reaction Buffer Pack (New England Biolabs, Cat. No. B9014S and M0273S) in a T100™
394 Thermal Cycler (Bio Rad) under the following conditions: one cycle at 95°C for 2.5 min,
395 followed by 35 cycles of 30 s at 95°C, 30 s at 55°C and 1 min at 68°C, with a final cycle
396 at 68°C for 5 min. The primers used for RT-PCR are listed in **Supplementary Table 4**.

397 **qRT-PCR**

398 Quantitative reverse transcription-polymerase chain reaction (qRT-PCR) was performed
399 with the SYBR Green method. The 25-fold diluted oligo dT or random hexamer priming
400 cDNA was amplified with the primers shown in **Supplementary Table 5** and was
401 performed with the CFX384™ Real-Time PCR System, in a C1000 Touch™ Thermal
402 Cycler (Bio-Rad) using iQ™ SYBR® Green Supermix (Bio-Rad, Cat. No. 1708882).
403 The results were normalized to the GAPDH, ATP5β, and HPRT reference genes and

404 measured by CFX Maestro software (Bio–Rad). Graphing and statistical analysis of qRT–
405 PCR results were performed using Prism 8 (GraphPad).

406 **Northern blotting**

407 Total RNA (10 µg) was separated on a 4% polyacrylamide (29:1) gel containing 8 M urea
408 at 20 W for 1 h and then transferred to a Hybond-N⁺ nylon transfer membrane (GE
409 Healthcare, Cat. No: RPN303B) at 400 mA for 1 h in 0.5X TBE buffer. RNA was cross-
410 linked to the membrane in a Stratalinker (Stratagene, 120 mJ). The blot was prehybridized
411 in Church buffer at 65°C (for hTR) or at 42°C (for oligonucleotide probe) for an hour.
412 Hybridizations with radiolabelled probes were performed in Church buffer at 65°C (for
413 hTR, probes were generated by nick translation of a polymerase chain reaction (PCR)
414 fragment with ³²P-α-dCTP) and 42°C (for oligonucleotide probe against 7SL, which was
415 labelled with ³²P-γ-ATP by T4 PNK kinase). The oligonucleotide sequences are listed in

416 **Supplementary Table 6.**

417 **Cell lysis and Western blotting**

418 All iPSC pellets were lysed in lysis buffer containing 0.5% CHAPS, 50 mM Tris-HCl
419 (pH 8.0), 50 mM KCl, 1 mM MgCl₂, 1 mM EGTA, 10% glycerol, 5 mM DTT, and 1 mM
420 PMSF. Total lysates were incubated at 4°C for 1 hr on a rotator, and insoluble material
421 was removed by centrifugation at 21,130 X g at 4°C for 10 min. Protein concentration
422 was measured using the protein assay dye (Bio–Rad, Cat. No. 5000006). Twenty
423 micrograms of protein were resolved on 4%-20% Bis-Tris gradient gels (GenScript, Cat.
424 No: M00657) at 180 V for 40 min and then transferred to polyvinylidene fluoride (PVDF)
425 membranes (BIO-RAD Immun-Blot®, Cat. #1620177) at 100 V for 1 hr. Five percent
426 skim milk in washing buffer was used as a blocking reagent. The prestained protein ladder
427 (Omics Bio, Cat: 02101-250) was used as a marker; α-tubulin (1:5000, ABclonal, Cat.

428 No: AC012) was used as a loading control. Cytiva software was used. The antibodies
429 used in this study are listed in **Supplementary Table 7**.

430 **Cytoplasmic/nuclear fractionation**

431 iPSCs (2×10^6) were washed with DPBS (Biological Industries, Cat. No: 02-023-1A) and
432 lysed in 50 μ l of fresh buffer A (0.05% Triton X-100, 10 mM HEPES-KOH, pH 7.9, 10
433 mM KCl, 1.5 mM MgCl₂, 10% glycerol, 0.34 M sucrose, 1 mM DTT, supplemented with
434 protease inhibitor cocktail) at 4°C for 10 min. The cytosolic fraction was collected and
435 clarified at 500 \times g at 4°C for 5 min twice. The cell monolayer was then washed three
436 times with DPBS and resuspended in a new buffer A. Both nuclear and cytoplasmic
437 fractions were analysed by Western blotting as mentioned before. The antibodies used in
438 this study are listed in **Supplementary Table 7**.

439 **Immunofluorescence assay**

440 The iPSCs were fixed with 4% paraformaldehyde at RT for 20 min, permeabilized with
441 0.1% Triton X-100 at RT for 5 min, and blocked with 1% BSA in DPBS at RT for an
442 hour, followed by incubation with the primary antibody against dyskerin (H-3) (Santa
443 Cruz Biotechnology, Cat. No. sc-373956, 1:500 dilution) at 4°C overnight. The slide was
444 washed three times with DPBS and then incubated with fluorescein (FITC)-conjugated
445 AffiniPure goat anti-mouse IgG (H+L) (Jackson ImmunoResearch, Cat. No. 115-095-003,
446 1:100 dilution) secondary antibody at 37°C for 1 hour. Nuclei were stained with
447 bisbenzimidazole H 33258 (Sigma–Aldrich, Cat. No. B2883-1 g, 1:1000 dilution) for 10 min
448 at 4°C after washing the cells with DPBS. After the indicated treatments, coverslips were
449 mounted on glass slides with Fluoromount™ Aqueous Mounting Medium (Sigma–
450 Aldrich, Cat. No. F4680-25ML) and photographed under an Axio Imager 2 fluorescence
451 microscope (ZEISS). Acquired images were quantified by using ImageJ/Fiji software.
452 Graphing and statistical analysis of the immunofluorescence assay results were

453 performed in Prism 8 (GraphPad). The antibodies used in this study are listed in
454 **Supplementary Table 8.**

455 **Data Availability**

456 Data will be uploaded after the manuscript is accepted.

457 **Acknowledgements**

458 We thank the patients and their families for participation in the research and all members
459 of the Tseng laboratory for helpful discussions. This work was supported by MOST 110-
460 2636-B-002-009 -, MOST 108-2321-B-002-050 -, MOST 110-2634-F-002-032 -, and
461 NTUH 111-T0008. We thank Dr. Yu-Lun Kuo and Fu-Mei, Hsieh at Biotools Co., Ltd.,
462 Taiwan, and Jung-Che Kuo at Pharmigene, Inc., Taiwan, for assisting with the scRNA-
463 seq analysis.

464 **Author Contributions**

465 C.-M.C., N.-C.L., and C.-K.T. designed the experiments. C.-M.C. performed most of the
466 experiments. H.-H.Y., E.-T.W., Y.-L.Y., Y.-H.C., and W.-L.H., provided clinical care
467 and phenotypic delineation of patients. W.-P.C. performed iPSC reprogramming. S.-Y.L.
468 performed karyotyping of iPSCs. N.-C.L. and W.-L.H. analysed the exome sequencing
469 results. C.-M.C. performed iPSC experiments. All authors analysed the data. C.-M.C. M.-
470 J.T., H.-H.Y., N.-C.L., and C.-K.T. wrote the manuscript.

471 **Competing interests**

472 The authors declare no competing interests.

References

1. Heiss, N.S. *et al.* X-linked dyskeratosis congenita is caused by mutations in a highly conserved gene with putative nucleolar functions. *Nature Genetics* **19**, 32-38 (1998).
2. AlSabbagh, M.M. Dyskeratosis congenita: a literature review. *J Dtsch Dermatol Ges* **18**, 943-967 (2020).
3. Aalfs, C.M., van den Berg, H., Barth, P.G. & Hennekam, R.C. The Hoyeraal-Hreidarsson syndrome: the fourth case of a separate entity with prenatal growth retardation, progressive pancytopenia and cerebellar hypoplasia. *Eur J Pediatr* **154**, 304-8 (1995).
4. Hreidarsson, S., Kristjansson, K., Johannesson, G. & Johannsson, J.H. A syndrome of progressive pancytopenia with microcephaly, cerebellar hypoplasia and growth failure. *Acta Paediatr Scand* **77**, 773-5 (1988).
5. Savage, S.A. Beginning at the ends: telomeres and human disease. *F1000Res* **7**(2018).
6. Aran, D. *et al.* Reference-based analysis of lung single-cell sequencing reveals a transitional profibrotic macrophage. *Nature Immunology* **20**, 163-172 (2019).
7. Moar, P. & Tandon, R. Galectin-9 as a biomarker of disease severity. *Cell Immunol* **361**, 104287 (2021).
8. Jorgovanovic, D., Song, M., Wang, L. & Zhang, Y. Roles of IFN-gamma in tumor progression and regression: a review. *Biomark Res* **8**, 49 (2020).
9. Hayden, M.S. & Ghosh, S. NF-kappaB in immunobiology. *Cell Res* **21**, 223-44 (2011).
10. Patel, A.A. *et al.* The fate and lifespan of human monocyte subsets in steady state and systemic inflammation. *J Exp Med* **214**, 1913-1923 (2017).
11. Ong, S.M. *et al.* The pro-inflammatory phenotype of the human non-classical monocyte subset is attributed to senescence. *Cell Death Dis* **9**, 266 (2018).
12. Metcalf, T.U. *et al.* Human Monocyte Subsets Are Transcriptionally and Functionally Altered in Aging in Response to Pattern Recognition Receptor Agonists. *J Immunol* **199**, 1405-1417 (2017).
13. Anbazhagan, K., Duroux-Richard, I., Jorgensen, C. & Apparailly, F. Transcriptomic network support distinct roles of classical and non-classical monocytes in human. *Int Rev Immunol* **33**, 470-89 (2014).
14. Swanson, K.V., Deng, M. & Ting, J.P. The NLRP3 inflammasome: molecular activation and regulation to therapeutics. *Nat Rev Immunol* **19**, 477-489 (2019).
15. Mao, L. *et al.* Loss-of-function CARD8 mutation causes NLRP3 inflammasome activation and Crohn's disease. *J Clin Invest* **128**, 1793-1806 (2018).

16. Rex, D.A.B. *et al.* A comprehensive pathway map of IL-18-mediated signalling. *J Cell Commun Signal* **14**, 257-266 (2020).
17. Wendt, K. *et al.* Gene and protein characteristics reflect functional diversity of CD56dim and CD56bright NK cells. *J Leukoc Biol* **80**, 1529-41 (2006).
18. Golden-Mason, L. *et al.* Galectin-9 functionally impairs natural killer cells in humans and mice. *J Virol* **87**, 4835-45 (2013).
19. Carter, R.H. & Fearon, D.T. CD19: lowering the threshold for antigen receptor stimulation of B lymphocytes. *Science* **256**, 105-7 (1992).
20. Shukla, S., Schmidt, J.C., Goldfarb, K.C., Cech, T.R. & Parker, R. Inhibition of telomerase RNA decay rescues telomerase deficiency caused by dyskerin or PARN defects. *Nat Struct Mol Biol* **23**, 286-92 (2016).
21. Tseng, C.K., Wang, H.F., Schroeder, M.R. & Baumann, P. The H/ACA complex disrupts triplex in hTR precursor to permit processing by RRP6 and PARN. *Nat Commun* **9**, 5430 (2018).
22. Wong, J.M., Kyasa, M.J., Hutchins, L. & Collins, K. Telomerase RNA deficiency in peripheral blood mononuclear cells in X-linked dyskeratosis congenita. *Hum Genet* **115**, 448-55 (2004).
23. Tseng, C.K. *et al.* Human Telomerase RNA Processing and Quality Control. *Cell Rep* **13**, 2232-43 (2015).
24. Boyraz, B. *et al.* Posttranscriptional manipulation of TERC reverses molecular hallmarks of telomere disease. *J Clin Invest* **126**, 3377-82 (2016).
25. Fok, W.C. *et al.* Posttranscriptional modulation of TERC by PAPD5 inhibition rescues hematopoietic development in dyskeratosis congenita. *Blood* **133**, 1308-1312 (2019).
26. Nagpal, N. *et al.* Small-Molecule PAPD5 Inhibitors Restore Telomerase Activity in Patient Stem Cells. *Cell Stem Cell* **26**, 896-909 e8 (2020).
27. Shukla, S., Jeong, H.C., Sturgeon, C.M., Parker, R. & Batista, L.F.Z. Chemical inhibition of PAPD5/7 rescues telomerase function and hematopoiesis in dyskeratosis congenita. *Blood Adv* **4**, 2717-2722 (2020).
28. Kondrashov, A. *et al.* Inhibition of polyadenylation reduces inflammatory gene induction. *RNA* **18**, 2236-50 (2012).
29. Wu, E.T. *et al.* Critical Trio Exome Benefits In-Time Decision-Making for Pediatric Patients With Severe Illnesses. *Pediatr Crit Care Med* **20**, 1021-1026 (2019).
30. McKenna, A. *et al.* The Genome Analysis Toolkit: a MapReduce framework for analyzing next-generation DNA sequencing data. *Genome Res* **20**, 1297-303 (2010).

31. Wang, K., Li, M. & Hakonarson, H. ANNOVAR: functional annotation of genetic variants from high-throughput sequencing data. *Nucleic Acids Res* **38**, e164 (2010).
32. Richards, S. *et al.* Standards and guidelines for the interpretation of sequence variants: a joint consensus recommendation of the American College of Medical Genetics and Genomics and the Association for Molecular Pathology. *Genet Med* **17**, 405-24 (2015).
33. Butler, A., Hoffman, P., Smibert, P., Papalexi, E. & Satija, R. Integrating single-cell transcriptomic data across different conditions, technologies, and species. *Nature Biotechnology* **36**, 411-420 (2018).
34. Stuart, T. *et al.* Comprehensive Integration of Single-Cell Data. *Cell* **177**, 1888-1902.e21 (2019).
35. Brennecke, P. *et al.* Accounting for technical noise in single-cell RNA-seq experiments. *Nat Methods* **10**, 1093-5 (2013).
36. Luecken, M.D. & Theis, F.J. Current best practices in single-cell RNA-seq analysis: a tutorial. *Mol Syst Biol* **15**, e8746 (2019).
37. Kobak, D. & Berens, P. The art of using t-SNE for single-cell transcriptomics. *Nature Communications* **10**, 5416 (2019).
38. Van der Maaten, L.J.P. & Hinton, G.E. Visualizing High-Dimensional Data Using t-SNE. *Journal of Machine Learning Research* **9**, 2579-2605 (2008).
39. Haghverdi, L., Lun, A.T.L., Morgan, M.D. & Marioni, J.C. Batch effects in single-cell RNA-sequencing data are corrected by matching mutual nearest neighbors. *Nat Biotechnol* **36**, 421-427 (2018).
40. Kinchen, J. *et al.* Structural Remodeling of the Human Colonic Mesenchyme in Inflammatory Bowel Disease. *Cell* **175**, 372-386.e17 (2018).
41. Aran, D. *et al.* Reference-based analysis of lung single-cell sequencing reveals a transitional profibrotic macrophage. *Nat Immunol* **20**, 163-172 (2019).
42. Yu, D., Huber, W. & Vitek, O. Shrinkage estimation of dispersion in Negative Binomial models for RNA-seq experiments with small sample size. *Bioinformatics* **29**, 1275-82 (2013).
43. Robinson, M.D., McCarthy, D.J. & Smyth, G.K. edgeR: a Bioconductor package for differential expression analysis of digital gene expression data. *Bioinformatics* **26**, 139-40 (2010).
44. Robinson, M.D. & Smyth, G.K. Small-sample estimation of negative binomial dispersion, with applications to SAGE data. *Biostatistics* **9**, 321-32 (2008).

Figure Legends

Figure 1. Clinical phenotype and telomere length measurement

a. Pedigree of the family. Unaffected individuals are shown as open shapes. The carrier is shown as a half-filled shape. Clinically affected individuals are shown as filled shapes. A deceased individual is shown as a shape with a diagonal line. Squares represent males. Circles represent females. **b** Telomere length measurement by quantitative PCR (qPCR) of peripheral blood cell genomic DNA from patients in the family and age-matched controls. Brain MRI showing cerebellar hypoplasia in the elder brother at 2.5 years old (**c**) and the younger brother at 1 year old (**e**). **d, f, g.** An abdominal computed tomography scan revealed hepatosplenomegaly in the elder brother at 1.3 years old (**d**) and in the younger brother at 3 years old (**f** and **g**).

Figure 2. Single-cell RNA-seq of PBMCs showing immunodeficiency in DC patients

a. t-distributed stochastic neighbour embedding (tSNE) analysis of PBMCs from the healthy donor (HD) and DC patient. A total of 4297 and 4286 single cells for the HD and DC subjects were clustered into five major clusters (B cells, CD4⁺ T cells, CD8⁺ T cells, monocytes, and NK cells). Cells were annotated by independently correlating each cell with reference transcriptomic datasets. **b.** Bar graph showing the percentage of each cell type relative to the total cell numbers in the healthy donor or DC patient. **c.** Enriched pathways by Reactome analysis in each immune cell subset. **d.** Heatmap of anti-pathogen

response genes in immune cells for the healthy donor and DC patient coloured by average fold change.

Figure 3. Single-cell RNA-Seq analysis reveals distinct contributions of monocyte and NK-cell populations in DC patients

a. Bar graph showing proportions of distinct monocyte subsets relative to their total monocyte counts in the healthy donor and DC patient, respectively. **b.** Violin plots showing the differential expression distribution of monocyte-associated genes between the healthy donor and DC patient in classical, intermediate, and nonclassical monocytes. **c.** Bar graph showing the proportions of the CD56^{bright} and CD56^{dim} subsets in the healthy donor and DC patient. **d.** Violin plots showing the differential expression distribution of NK-cell-associated genes between the healthy donor and DC patient.

Figure 4. The DC patient exhibits defects in B-cell function

a. Bar graph showing CD4⁺ T and CD8⁺ T-cell proportions in the healthy donor and DC patient. **b.** Bar graph showing distinct B-cell subset proportions in the healthy donor and DC patient. **c.** Violin plots showing the differential expression levels of B-cell marker genes in B cells between the healthy donor and DC patient.

Figure 5. DKC1_R449G iPSCs exhibit a shorter telomere length, reduced levels of hTR, and mislocalized DKC1

a. Telomere lengths determined by Southern blot TRF analysis of gDNA prepared from WT_iPSC, WT_iPSC_F, R449G_iPSC_1 and R449G_iPSC_2 cells. **b.** Western blot

analysis of cell lysates from WT_iPSC, WT_iPSC_F, R449G_iPSC_1 and R449G_iPSC_2 cells. TUBULIN served as a loading control. **c.** Northern blot analysis of hTR from WT_iPSC, WT_iPSC_F, R449G_iPSC_1 and R449G_iPSC_2 cells. A probe against 7SL RNA served as a loading control. **d.** Western blot analysis of nuclear and cytosolic fractions from WT_iPSC, WT_iPSC_F, R449G_iPSC_1 and R449G_iPSC_2 cells. Lamin A/C served as a nuclear marker, and GAPDH served as a cytosolic marker. **e.** Immunofluorescence of DKC1 in WT_iPSC_F and R449G_iPSC_1 cells. The scale bar represents 10 μ m. **f.** Bar graph illustrating the distribution of DKC1 in the cytosolic and nuclear fractions.

Figure 6. Inhibition of oligoadenylation of hTR restores telomere length in DKC1 mutant iPSCs

a. Northern blot analysis of hTR from WT_iPSC_F, R449G_iPSC_1 and R449G_iPSC_2 cells treated with RG7834, Cordycepin, or DMSO. A probe against 7SL RNA served as a loading control. **b.** Total RNA prepared from WT_iPSC_F and R449G_iPSC_1 cells treated with RG7834, Cordycepin, or DMSO was subjected to qRT-PCR for oligoadenylated hTR. Bar graph of the mean fold change relative to DMSO-treated samples and normalized to GAPDH, ATP5b, and HPRT. Mean values were calculated from triplicate qRT-PCR experiments with three biological replicates, with bars representing the SE. **c.** Telomere lengths determined by Southern blot TRF analysis of gDNA prepared from WT_iPSC_F and R449G_iPSC_1 treated with RG7834, Cordycepin, or DMSO. **d.** Schematic illustrating the dysfunction of DKC1_R449G in telomere maintenance.

Supplemental Tables

Table 1. Laboratory features of two patients with HHS

Age (yr)	Elder brother	Younger brother	Reference
----------	---------------	-----------------	-----------

WBC (/μL)	1.6	-	7240	5000-17000 (age 1-6)
	2.8	1050 L	7450	
	3	2560 L	7620	
	3.5	-	3060 L	
	5.7	-	1030 L	
Hb (g/dL)	1.6	-	13.8 L	11.5-14 (age 1-6)
	2.8	9.8 L	10.1 L	
	3	2.6 L	12.6	
	3.5	-	10.3 L	
	5.7	-	8.6 L	
PLT (k/μL)	1.6	-	102 L	150-400 (age 1-6)
	2.8	35 L	40 L	
	3	4 L	107 L	
	3.5	-	76 L	
	5.7	-	36 L	
Neutrophils (/μL)	1.6	--	4699	1000-8500 (age 1-6)
	2.8	473 L	6362	
	3	2289	5600	
	3.5	-	1888	
	5.7	-	900 L	
Lymphocytes (/μL)	1.6	-	1499 L	2180-8270 (age 1-2)
	2.8	74 L	693 L	2400-5810 (age 2-5)
	3	90 L	1227 L	
	3.5	-	930 L	
	5.7	-	50 L	
Monocytes (/μL)	1.6	-	557	200-1000 (age 1-6)
	2.8	158 L	261	
	3	161 L	617	
	3.5	-	211	
	5.7	-	70 L	
CD3 ⁺ T cells (/μL)	2.8	64.8 L	857.5 L	1610-4230 (age 2-5)
	3.5	-	865.1 L	
CD4 ⁺ T cells (/μL)	2.8	46.8 L	551.2 L	900-2860 (age 2-5)
	3.5	-	567.5 L	
Naïve CD4 ⁺ CD45RA ⁺ T cells (/μL)	2.8	43.2 L	408.3	300-2300 (age 2-5)
	3.5	-	460.5	
CD8 ⁺ T cells (/μL)	2.8	16.5 L	316.4 L	630-1910 (age 2-5)
	3.5	-	279.1 L	
CD19 ⁺ B cells (/μL)	2.8	0.5 L	122.5 L	700-1300 (age 2-5)
	3.5	-	46.5 L	
CD56 ⁺ NK cells (/μL)	2.8	6.0 L	20.4 L	61-510 (age 2-5)
	3.5	-	18.6 L	

IgG (mg/dL)	2.5	337.0 L	-	419-1274 (age 2-3)
	2.8	673	774	
	3.5	-	1150	569-1597 (age 3-5)
	5.3	-	1050	
IgA (mg/dL)	2.8	110	33.4	19-235 (age 2-3)
	3.5	-	38.1	55-152 (age 3-5)
	5.3	-	25.9 L	
IgM (mg/dL)	2.8	37.6	133 H	28-113 (age 2-3)
	3.5	-	309 H	22-100 (age 3-5)
	5.3	-	118	

Abbreviations: high, H; low, L

Supplementary Table 2. Primers for sequencing the human *DKC1* gene

Name	Sequence	Target
CKOligo-315	FW: TCAAGGCTTCTTGGATTTGG	DKC1
CKOligo-316	RV: AAGAGTAACAAAGCTGGTAC	

Supplementary Table 3. qPCR primers and standard templates list

Name	Oligomer sequence (5' – 3')	Description
CKOligo-237	TTAGGGTTAGGGTTAGGGTTAGGGTTAG GGTTAGGGTTAGGGTTAGGGTTAGGGTT AGGGTTAGGGTTAGGGTTAGGGTTAGGG	Telomere Standard
CKOligo-238	CAGCAAGTGGGAAGGTGTAATCCGTCTC CACAGACAAGGCCAGGACTCGTTTGTAC CCGTTGATGATAGAATGGG	36B4 (SCG) Standard
CKOligo-239	CGGTTTGTTTGGGTTTGGGTTTGGGTTT GGTTTGGGTT	Telomere-F
CKOligo-240	GGCTTGCCTTACCCTTACCCTTACCCTTA CCCTTACCCT	Telomere-R
CKOligo-241	CAGCAAGTGGGAAGGTGTAATCC	36B4 (SCG)-F
CKOligo-242	CCCATTCTATCATCAACGGGTACAA	36B4 (SCG)-R

Supplementary Table 4. Primers used for RT-PCR

Name	Sequence	Target
Oct4	F: TGTACTCCTCGGTCCCTTTC	<i>Oct4</i>
	R: TCCAGGTTTTCTTTCTAGC	
Sox2	F: GCTAGTCTCCAAGCGACGAA	<i>Sox2</i>
	R: GCAAGAAGCCTCTCCTTGAA	
Nanog	F: CAGTCTGGACACTGGCTGAA	<i>Nanog</i>
	R: CTCGCTGATTAGGCTCCAAC	

Supplementary Table 5. Primers used for qRT-PCR

Name	Sequence	Target
CKOligo-14	FW: GCGAAGAGTTGGGCTCTGTCA	Total hTR
CKOligo-15	RV: TTCCTCTCCTGCGGCCTGAAA	
CKOligo-16	FW: CTTTCAGGCCGCAGGAAGAGGAA	Extended hTR
CKOligo-17	RV: GGTGACGGATGCGCACGAT	
CKOligo-18	FW: TGCTGAGGATTTGGAAAGGG	HPRT
CKOligo-19	RV: ACAGAGGGCTACAATGTGATG	
CKOligo-20	FW: GATCCTCTAGACTCCACCTCTC	ATP5 β
CKOligo-21	RV: AGAAAGTTCATCCATACCCAGG	
CKOligo-22	FW: ACATCGCTCAGACACCATG	GAPDH
CKOligo-23	RV: TGTAGTTGAGGTCAATGAAGGG	
CKOligo-441	FW: AGGACTAAGAAGGCTGAGTC	SCARNA4
CKOligo-442	RV: GAGTGTTGGGTAGTACAGTC	
CKOligo-445	FW: GGAGGCTGATACACAAATTG	SCARNA8
CKOligo-446	RV: GTATCTGTCCGTTACGATTTC	

CKOligo-449	FW: ATACTCCAGAGGAAGCTGAG	SCARNA13
CKOligo-450	RV: TCTCGACTGCAAAGCTTCTC	
CKOligo-455	FW: AAGCCAGCCAATGAATCTGC	SNORA33
CKOligo-456	RV: TTGTTATAGCCATTCTCAGGG	
CKOligo-458	FW: GAGCACTTTCACAGGTCCTC	SNORA37
CKOligo-457	RV: GTCCCATTGAATGACAGCTG	
CKOligo-459	FW: GGATTCAGACTACAATATAGC	SNORA63
CKOligo-460	RV: CATGTATGAGACCAAGCGTC	
CKOligo-461	FW: ACTCTCTCGGCTCTGCATAG	SNORA64
CKOligo-462	RV: GCCTGTTGCACCCCTCAAG	
CKOligo-463	FW: CACTGCACCTGACCAGGTC	SNORA65
CKOligo-464	RV: CATGCTTTCGGCACAGAGTC	
CKOligo-465	FW: TTGCACCTAAACCCAAGAATC	SNORA68
CKOligo-466	RV: AGTTGTGGAACCTCCAAATTC	
CKOligo-467	FW: GGGTCAATCTGCAGCGCTAG	SNORA76
CKOligo-468	RV: CTTGTCGCTCGCGGTAAAAAG	
CKOligo-451	FW: CAAGCCTCCAGCGTGCTTG	SNORA9
CKOligo-452	RV: CATTGTCTGAAATTTCTATAACC	

Supplementary Table 6. Oligonucleotides for probe preparation for Northern blotting

Name	Sequences		Target
CKOligo-1	FW	GGGTTGCGGAGGGTGGGC	hTR probe generated by PCR
CKOligo-2	RV	CCGACTTTGGAGGTGCCTTC	
CKOligo-5	GGAGGTCACCATATTGATGCCGAAGTACTAGT		7SL probe

CKOligo-7	GCGAACGCAGTCCCCACTACCACAAATTA	Human U1 probe
CKOligo-8	GGTCGATGCGTGGAGTGGACGGAGC	Human U2 probe
CKOligo-9	CTCAGACCGCGTTCTCTCCCTCTCACTCCCCAA T	Human U3 probe
CKOligo-10	CGCGCCTCGGATAGACCTCATTGGCTACG	Human U4 probe
CKOligo-11	GGGTTAAGACTCAGAGTTGTTCTCTCCACGG	Human U5 probe
CKOligo-12	ATGGAACGCTTCACGAATTTGC	Human U6 probe
CKOligo-452	CATTGTCTGAAATTTCTATAACC	SNORA9
CKOligo-456	TTGTTATAGCCATTCTCAGGG	SNORA33
CKOligo-460	CATGTATGAGACCAAGCGTC	SNORA63
CKOligo-464	CATGCTTTCGGCACAGAGTC	SNORA65
CKOligo-466	AGTTGTGGAACCTCCAAATTC	SNORA68
CKOligo-468	CTTGTCGCTCGCGGTTAAAAAG	SNORA76

Supplementary Table 7. Antibodies for Western blotting

Antibodies	Source	Cat. No.	Dilution
Loading control			
α -Tubulin	ABclonal	AC012	1:5000
Nuclear and cytosolic marker			

Lamin A/C	ABclonal	A19524	1:50000
GAPDH	ABclonal	AC027	1:100000
Secondary antibody			
Goat anti-Mouse IgG- h+1 DyLight® 680 conjugated	Bethyl Laboratories	A90-516D6	1:5000
Goat anti-Rabbit IgG (H+L)-HRP	CROYEZ	C04003	1:5000
Primary antibody			
DKC1	Bethyl Laboratories	A302-591A	1:2000
NOP10	ABclonal	A18250	1:1000
NHP2	Proteintech Group	15128-1-AP	1:500
TERT	Abcam	ab32020	1:1000

Supplementary Table 8. Antibodies used for immunofluorescence assays

Antibodies	Source	Cat. No.	Dilution
Primary antibody			
Dyskerin (H-3)	Santa Cruz Biotechnology	sc-373956	1:500
Secondary antibody			
Fluorescein (FITC)- conjugated AffiniPure Goat Anti-Mouse IgG (H+L)	Jackson ImmunoResearch	115-095-003	1:100

Supplemental Figure Legends

Supplementary figure 1. Genomic characterization of our patient

a. Exome sequencing showing the inheritance of the DKC1 mutation from the mother to the sibling. **b.** Sanger sequencing of DKC1 gDNA prepared from PBMCs of all members of the family. The patient's father is indicated by C (normal). The patient's mother and sibling are indicated to have a DKC1 c.1345C> G (p. R449G) mutation.

Supplementary figure 2. DKC1 domain and conservation in different species

a. Schematic diagram of the DKC1 protein with known domains, including the nuclear localization signal (NLS). The R449G mutation identified in this study is indicated with a red arrow. NLS: nuclear localization; TruB (PUS) domain: pseudouridine synthase domain; PUA domain: pseudouridine synthases & archaeosine-specific transglycosylases domain. **b.** Conservative analysis shows a high degree of conservation of the arginine 449-containing portion in the DKC1 protein from other species. Arginine 449 is highlighted. The red border indicates the nuclear localization signal.

Supplementary figure 3. Derivation and characterization of DKC1 mutant iPSCs

a. Bright-field images of WT_iPSC, WT_iPSC_F, R449G_iPSC_1 and R449G_iPSC_2 cells. **b.** RT-PCR of pluripotency-associated gene expression in WT_iPSC, WT_iPSC_F, R449G_iPSC_1 and R449G_iPSC_2 cells. **c.** Sanger sequencing of codons 1342–1350 of WT_iPSC, WT_iPSC_F, R449G_iPSC_1 and R449G_iPSC_2 cells. c.1345C> G (p.

R449G) mutation is indicated by the arrow. **d.** Metaphase G-banding karyotyping of iPSCs as indicated.

Figures

Figure 1

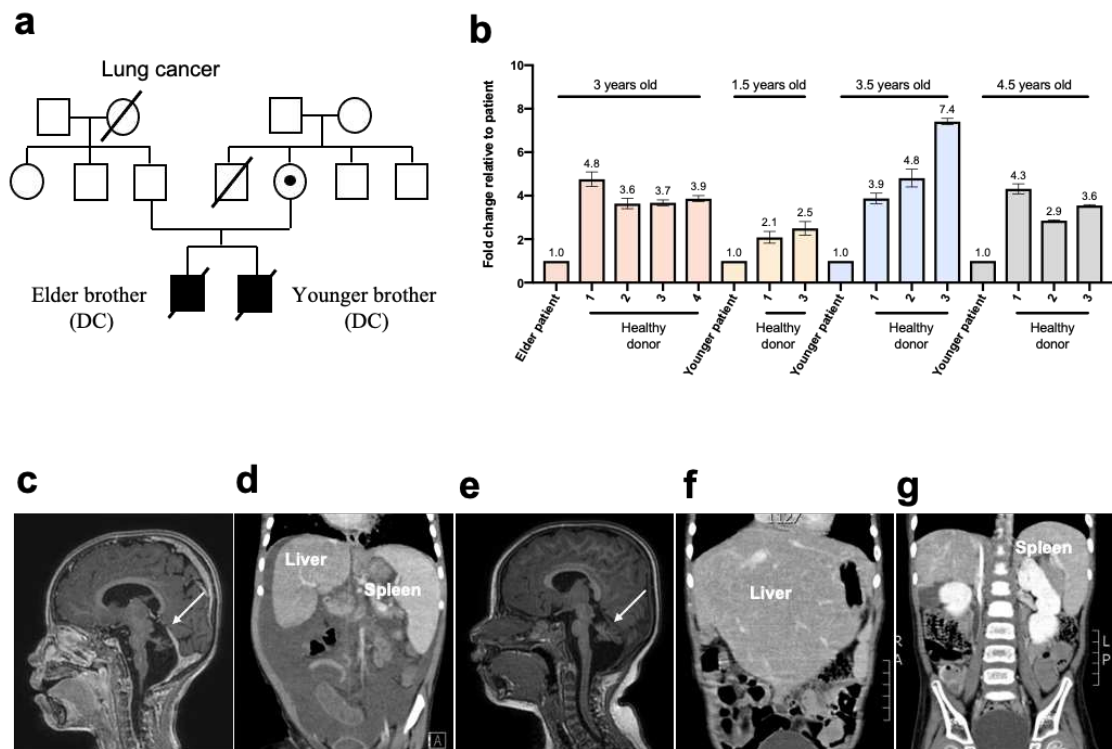


Figure 2

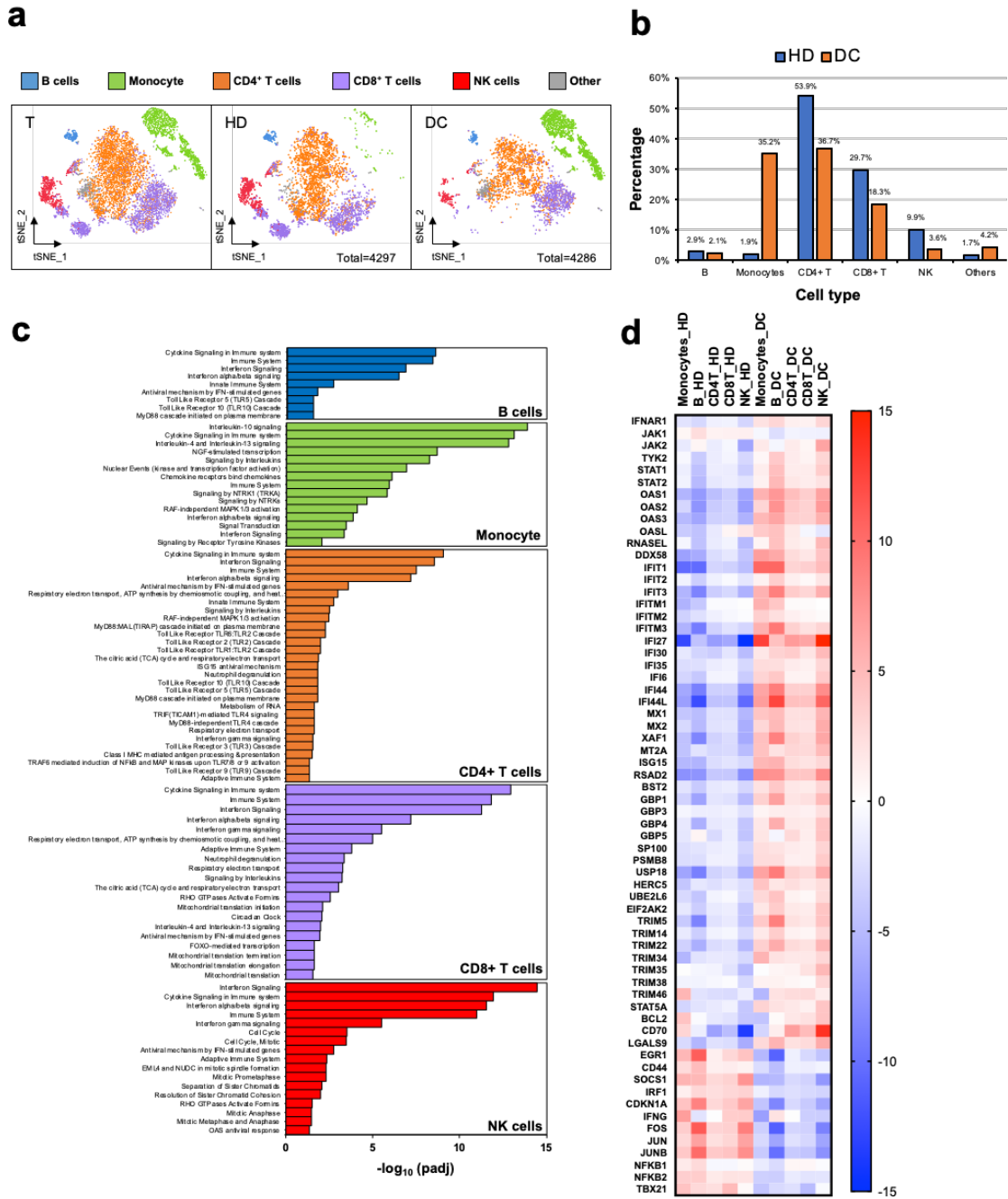


Figure 3

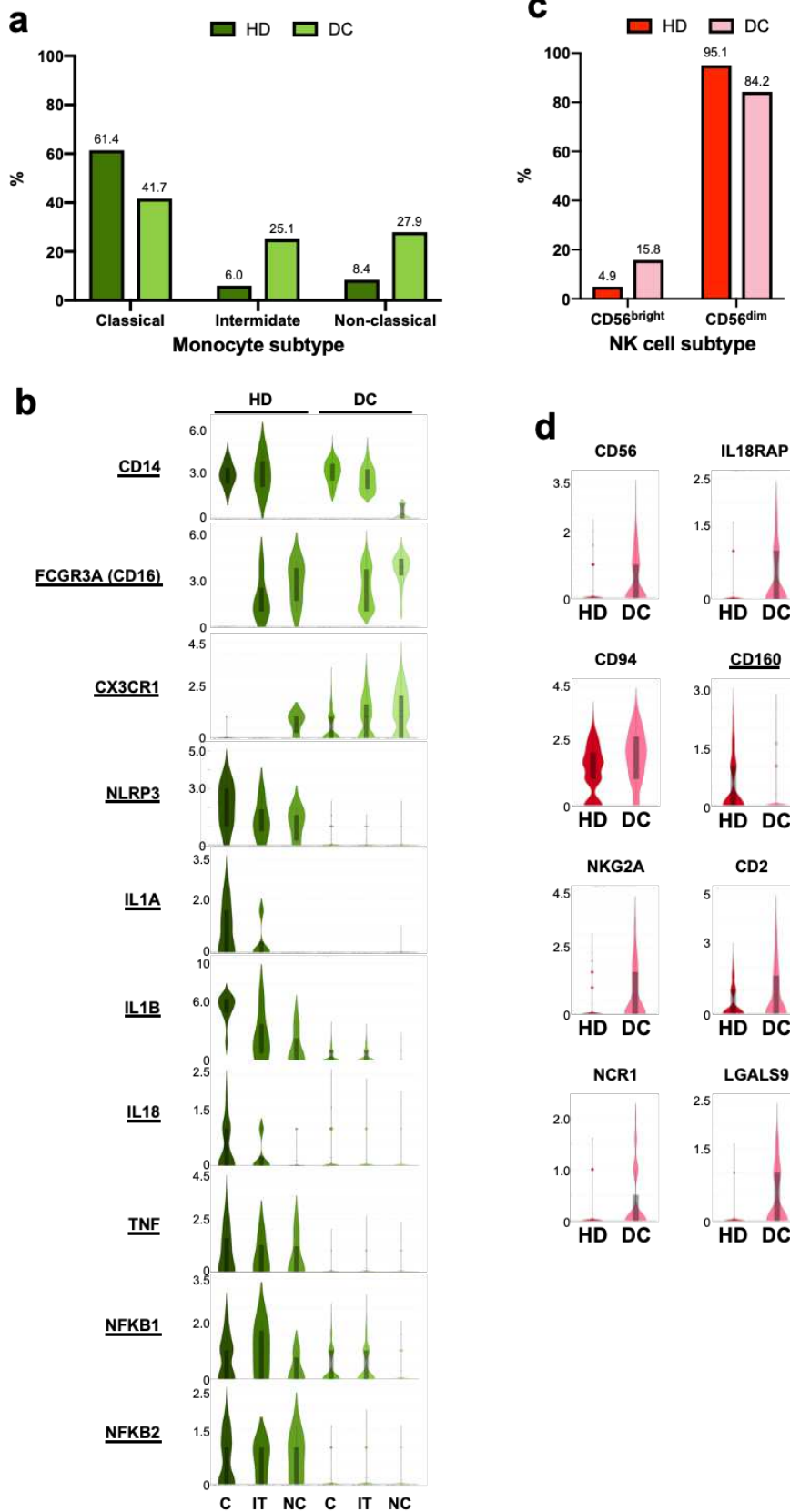


Figure 4

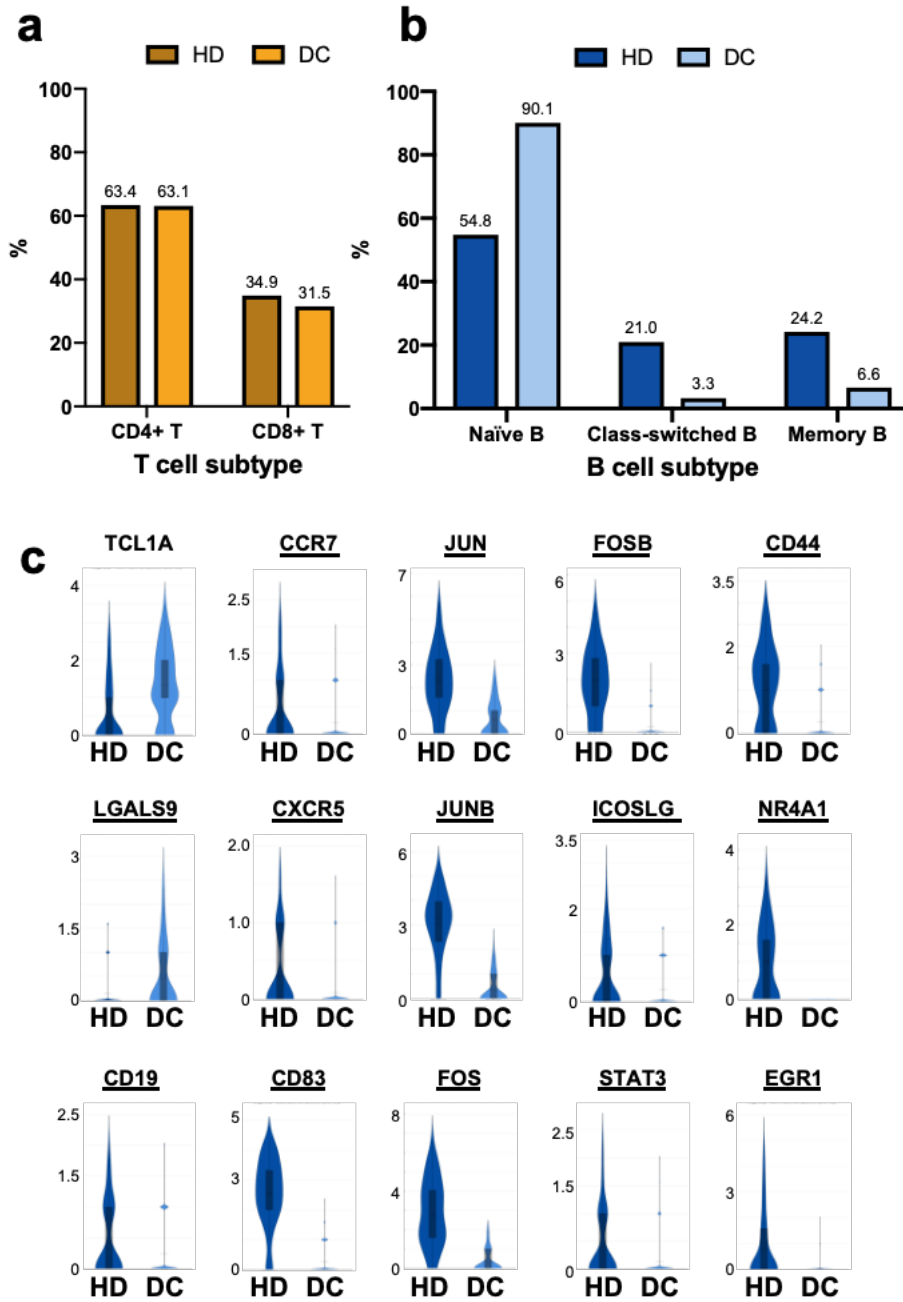


Figure 5

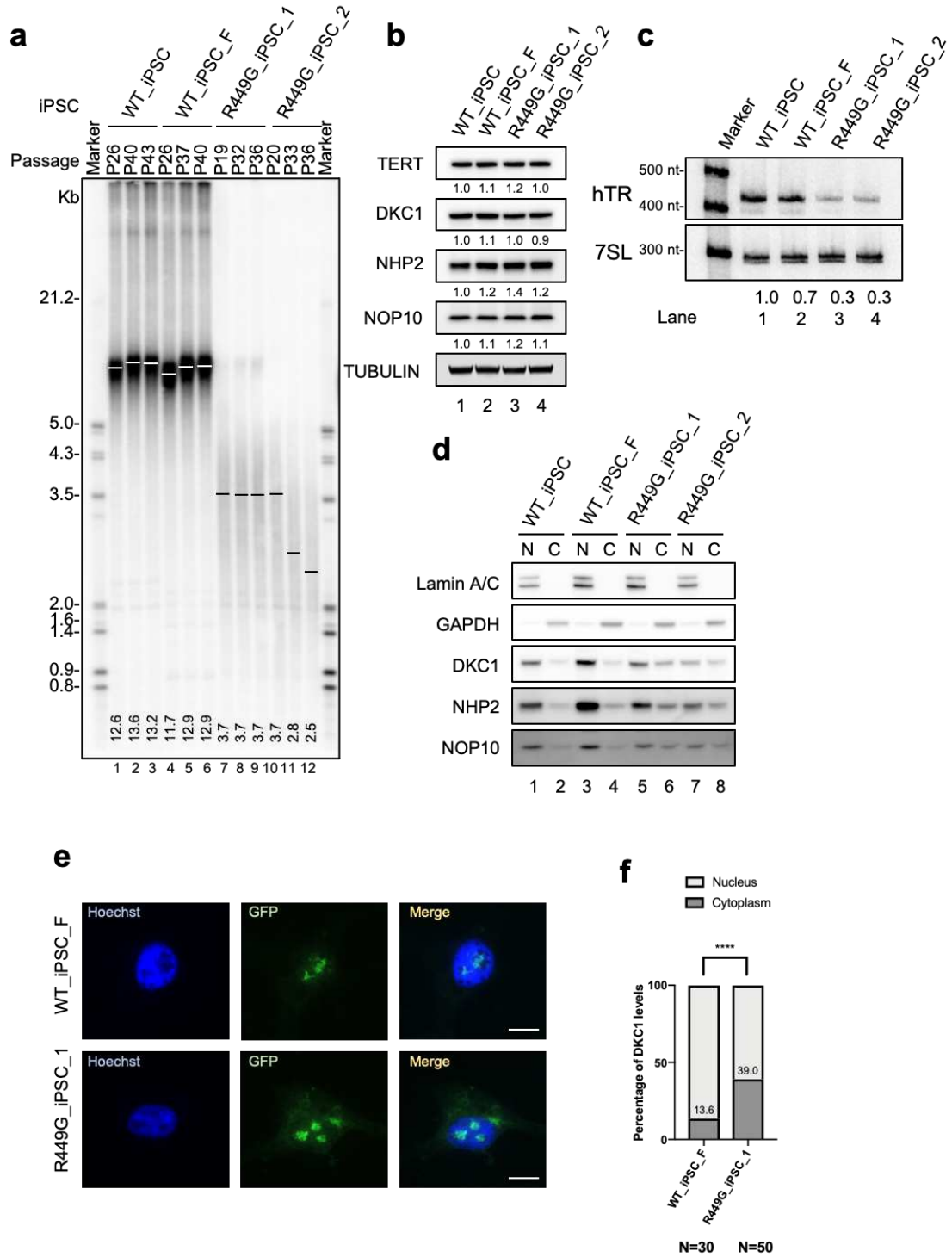
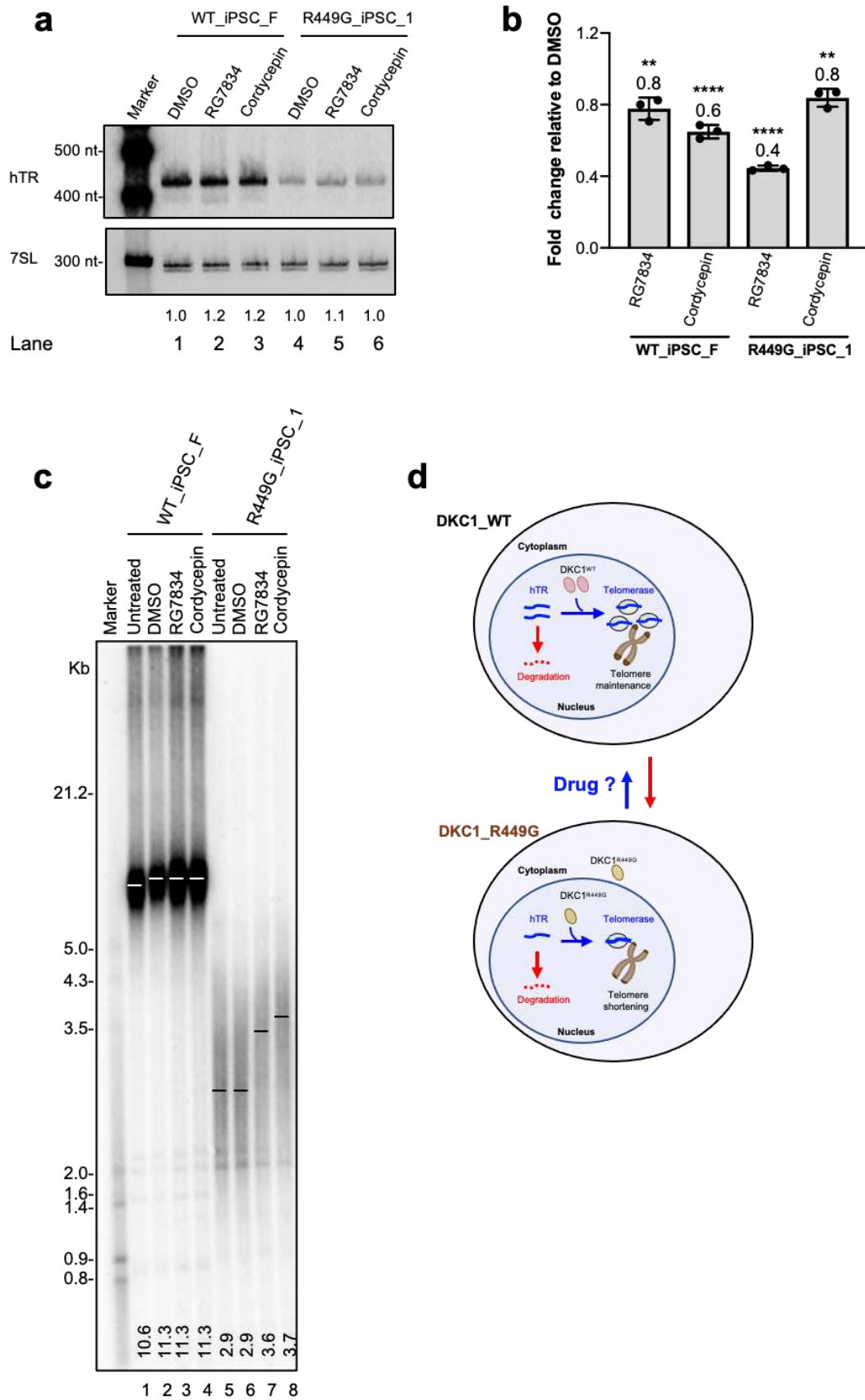
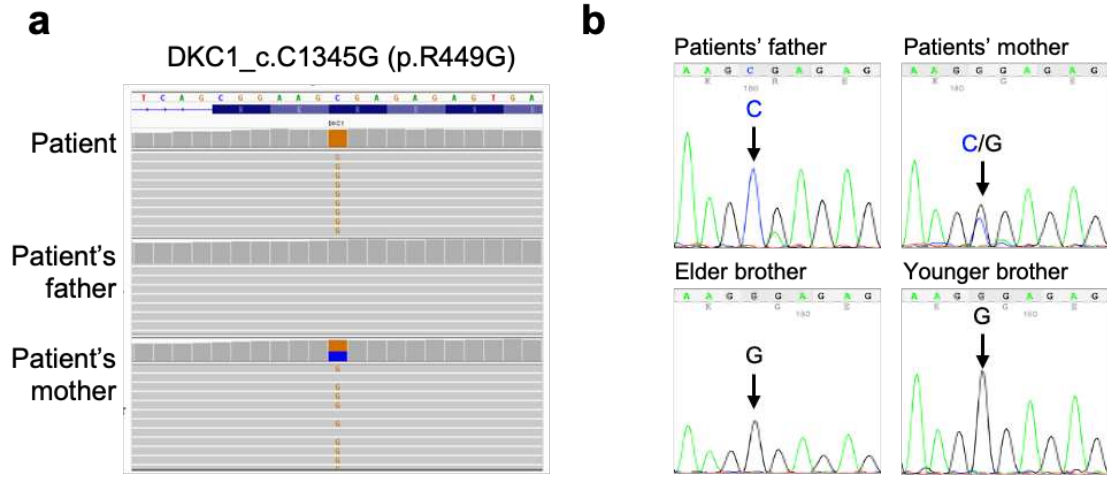


Figure 6

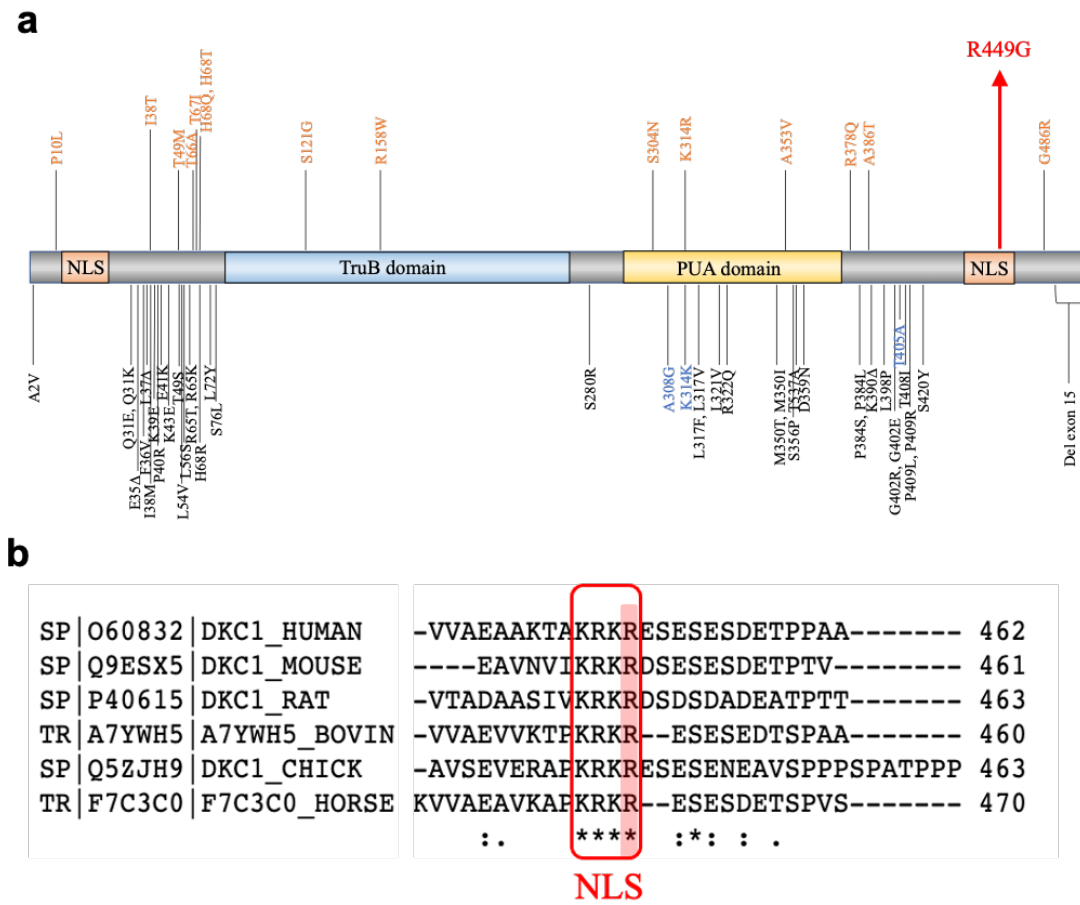


Supplemental Figure

Figure 1

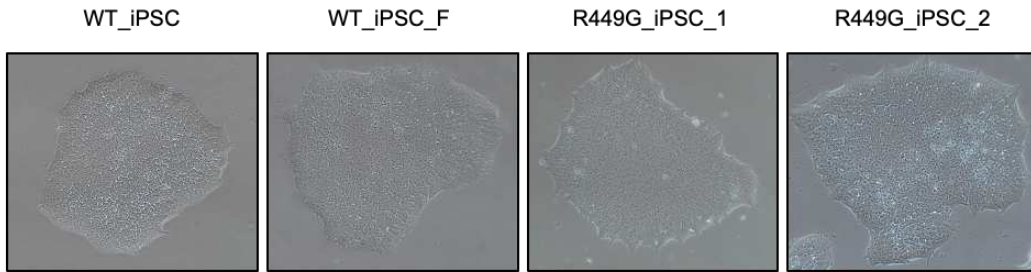


Supplementary Figure 2

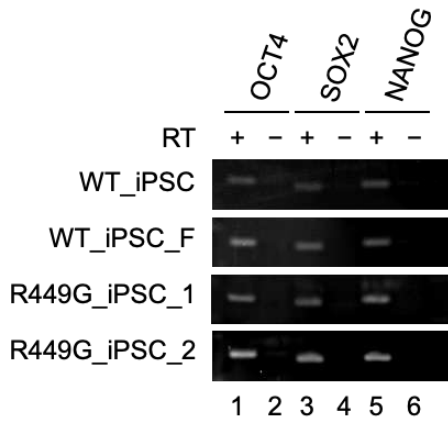


Supplementary Figure 3

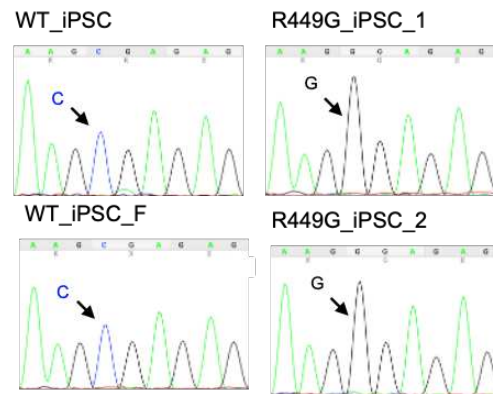
a



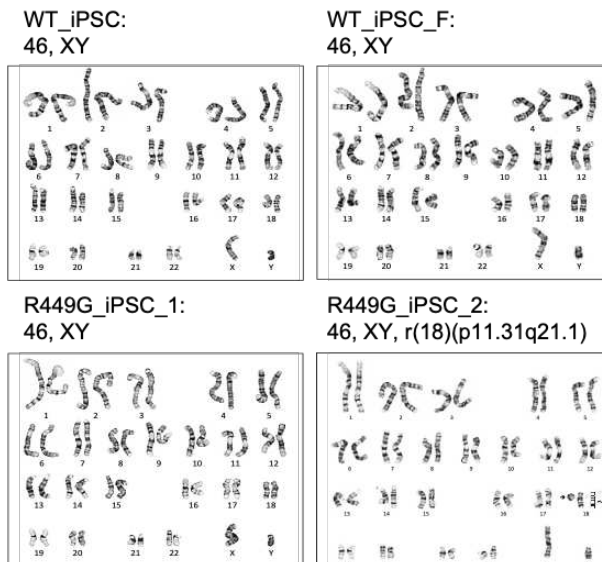
b



c



d



Supplementary Files

This is a list of supplementary files associated with this preprint. Click to download.

- [3.SupplementaryInformation.pdf](#)